Small

NANO · MICRO small
www.small-journal.com

RESEARCH ARTICLE

Realizing Highly Reversible $Nb^{5+}/Nb^{4+}/Nb^{3+}$ Redox Reactions in Bulk NASICON-$NaNbAl(PO_4)_3$ Anode Under Higher Current Rates

Ayon Phukan[1] | Biplab Patra[1] | Tanushree Acharya[2] | Suraj Halder[3] | Swathy Narayanan[1] | Sheetal Kumar Jain[3] | Gopalakrishnan Sai Gautam[2] | Premkumar Senguttuvan[1]

[1]New Chemistry Unit, International Centre for Materials Science, and School of Advanced Materials, Jawaharlal Nehru Centre For Advanced Scientific Research, Bangalore, Karnataka, India | [2]Materials Engineering, Indian Institute of Science, Bangalore, Karnataka, India | [3]Solid-State and Structural Chemistry Unit, Indian Institute of Science, Bangalore, Karnataka, India

Correspondence: Premkumar Senguttuvan (prem@jncasr.ac.in)

Received: 18 August 2025 | **Revised:** 16 January 2026 | **Accepted:** 27 January 2026

Keywords: multi-redox activity | $NaNbAl(PO_4)_3$ | NASICON anode | reversible $Nb^{5+}/Nb^{4+}/Nb^{3+}$ | sodium-ion battery

ABSTRACT

Natrium SuperIonic CONductor (NASICON)-$Nb_2(PO_4)_3$ is regarded as a potential anode for sodium-ion batteries due to its higher storage capacity (~150 mAh g^{-1}) stemming from two-electron $Nb^{5+}/Nb^{4+}/Nb^{3+}$ redox. However, the reversibility of $Nb^{5+}/Nb^{4+}/Nb^{3+}$ redox is limited by its structural degradation. Herein, we unveil highly reversible $Nb^{5+}/Nb^{4+}/Nb^{3+}$ redox reactions in bulk NASICON-$NaNbAl(PO_4)_3$ (NaNbAl) anode. The introduction of Na-ions via Al^{3+} substitution stabilizes the NASICON framework and activates distinct Nb redox couples with Na (de)intercalation, as demonstrated via our density functional theory-based calculations. This bulk anode delivers capacities up to 90 mAh g^{-1} at 5C with 86% retention after 1000 cycles. More significantly, we capture rapid sodium ion (de)intercalation in NaNbAl at high current rates using operando synchrotron X-ray diffraction which is in agreement with the calculated low migration barriers associated with Na motion within the structure. A full Na-ion cell ($Na_4V_2(PO_4)_3$||NaNbAl) achieves an energy density of 201 Wh kg^{-1} (based on cathode mass) and retains 84% capacity over 200 cycles at 1C. This study opens new avenues for realizing reversible $Nb^{5+}/Nb^{4+}/Nb^{3+}$ redox in bulk NASICON anodes with suitable chemical substitutions.

1 | Introduction

Sodium-ion batteries (SIBs) have emerged as promising next-generation energy storage devices due to the inexpensive and widespread availability of sodium resources [1, 2]. The first-generation SIB prototypes utilize layered transition metal oxides [3], Prussian blue analogues [4], and polyanionic materials [5–7] as cathodes, whereas hard carbon remains as the leading anode candidate. Hard carbon stores sodium ions closer to 0.1 V versus Na^+/Na^0 with storage capacities of 200–350 mAh g^{-1} [8]. However, it suffers from lower initial Coulombic efficiency (ICE), the risk of sodium metal plating during rapid charging, and limited volumetric energy density [9, 10], prompting the exploration of alternative anode materials.

NASICON (NAtrium SuperIonic CONductor)-type anodes have been explored as potential alternatives owing to their robust structural stability and high sodium-ion diffusivity [11–16]. $NaTi_2(PO_4)_3$and $Na_3V_2(PO_4)_3$ anodes suffer from higher insertion voltage (~2.1 V) and lower capacity (~60 mAh g^{-1}), respectively,

Ayon Phukan and Biplab Patra contributed equally to this work.

leading to lower energy density SIBs [12, 17]. To address these challenges, we previously developed a multi-electron bulk $Nb_2(PO_4)_3$ anode, achieving a reversible capacity of ~150 mAh g^{-1} at a lower insertion voltage (~1.4 V) [18]. Yet, the reversibility of $Nb^{5+}/Nb^{4+}/Nb^{3+}$ redox reactions in the $Nb_2(PO_4)_3$ anode is limited by the distortion of NbO_6 octahedra and structural instability during the extensive cycling. Consequently, it exhibited poor capacity retention (60.2% after 200 cycles). To overcome these limitations, a "Na-filled" $Na_{1.5}V_{0.5}Nb_{1.5}(PO_4)_3$ anode was subsequently developed, delivering ~140 mAh g^{-1} with 89% capacity retention over 500 cycles [14]. Nano-scale NASICON anodes $NaVNb(PO_4)_3$ [15], $NaCrNb(PO_4)_3$ [16] and $NaV_{0.25}Al_{0.25}Nb_{1.5}(PO_4)_3$ [19] have also been investigated, offering capacities of 150–200 mAh g^{-1} with improved cycling stability. Nevertheless, a fundamental understanding of the reversibility of the two-electron $Nb^{5+}/Nb^{4+}/Nb^{3+}$ redox process in NASICON-type anodes remains elusive, largely due to the overlapping V and Cr redox activities.

To this end, we design a bulk anode material, namely NASICON-$NaNbAl(PO_4)_3$ (NaNbAl), wherein the incorporation of sodium ions *via* electrochemically inactive Al^{3+} substitution is expected to stabilize the anode structure during two-electron $Nb^{5+}/Nb^{4+}/Nb^{3+}$ redox reactions. This strategy was inspired by the $V^{5+}/V^{4+}/V^{3+}$ redox activation in $Na_3VCr(PO_4)_3$ and $Na_3V_{1.5}Al_{0.5}(PO_4)_3$ cathodes [20, 21]. Notably, the $V^{5+}/V^{4+}/V^{3+}$ two-electron reactions in NASICON cathodes are less reversible due to VO_6 distortion [22, 23] and V^{5+} migration [24, 25]. On the contrary, niobium cations (Nb^{5+}, $Nb^{4+,}$ and Nb^{3+}) are more electropositive than their vanadium counterparts. Therefore, they produce strong covalent bonds with oxygen and reduce NbO_6 distortion and stabilize the NASICON framework [26] as observed from X-ray absorption spectroscopy (XAS) measurements, which are in agreement with our density functional theory (DFT) based calculations as well. Accordingly, the NaNbAl anode displays reversible $Nb^{5+}/Nb^{4+}/Nb^{3+}$ redox reactions even at higher current rates, as observed by combined electrochemical and *operando* XRD measurements and in agreement with our Na^+ migration barriers (E_m) calculated with DFT-based nudged elastic band (NEB) calculations.

2 | Results and Discussion

We synthesized NASICON-$NaNbAl(PO_4)_3$ through conventional solid-state reaction entirely in air, unlike previous Nb-based NASICONs that required an inert atmosphere (for details, see Supporting Information). The X-ray diffraction (XRD) pattern of the NaNbAl anode (Figure 1a) can be indexed with $R\bar{3}c$ space group, with a minor impurity of $AlPO_4$ (~5%). Despite our efforts, phase-pure NaNbAl could not be obtained (Figure S1). The XRD pattern was refined, and the corresponding crystallographic parameters (a = 8.4801(1) Å; c = 21.7865(0) Å; V = 1356.81(6) $Å^3$) matched well with previous reports (Table S1) [27, 28]. The crystal structure of NaNbAl is built by lantern units composed of two $(Nb/Al)O_6$ and three PO_4 units, which are stacked along the c-axis (inset of Figure 1a). Based on our XRD refinement, the total sodium content in NaNbAl was estimated as 0.978, with Na(1) and Na(2) occupancies of 0.858 and 0.04, respectively. Scanning electron microscopy (SEM) images reveal the presence of cube-like micron-sized bulk particles (~1–2 μm) (Figure 1b) in the NaNbAl anode. Further, the high-resolution transmission electron microscopy (HRTEM) image displays a cubic-like particle (Figure 1c) with a lattice fringe spacing of 6.1 Å, corresponding to (012) lattice plane (Figure 1d). To assess the oxidation state of Nb in NaNbAl, X-ray absorption spectroscopy measurements were performed along with Nb_2O_5 and NbO_2 references. Their corresponding normalized X-ray absorption near-edge structure (XANES) spectra, collected at the Nb K-edge, are shown in Figure S2a. The absorption edge position of NaNbAl closely matches that of Nb_2O_5, thereby confirming the exclusive presence of Nb^{5+} in the NASICON lattice. Moreover, X-ray photoelectron spectroscopy (XPS) measurements also confirmed the exclusive presence of Nb^{5+} in the NASICON lattice (Figure S2b). The uniform distribution of elements is confirmed by high-angle annular dark-field (HAADF) scanning transmission electron microscopy (STEM) elemental mapping (Figure 1e).

The electrochemical Na-ion storage performance of NaNbAl anode was evaluated against sodium metal at C/10 rate in the voltage window of 3.0–0.9 V (Figure 2a). The theoretical capacity of NaNbAl is estimated to be ~125 mAh g^{-1} based on $Nb^{5+}/Nb^{4+}/Nb^{3+}$ two-electron reactions. The anode showed an intriguing two-step voltage-capacity profile at ~1.8 and 1.1 V versus Na^+/Na^0. Its first discharge/charge capacities are estimated as 138/122 mAh g^{-1} with an initial coulombic efficiency of 87.7%, thereby accounting for a reversible insertion of 2 Na^+ per formula unit (*pfu*) (Figure 2a). From the next cycle onwards, the NaNbAl anode delivers reversible capacities of ~125 mAh g^{-1}. The corresponding dQ/dV profiles display redox peaks at 2.2 and 1.8 V (Figure 2b), attributable to the Nb^{5+}/Nb^{4+} couple, whereas the sharp peaks located at 1.1 V are attributed to the Nb^{4+}/Nb^{3+} redox couple, consistent with previous reports [19, 29]. The NaNbAl anode maintained a good capacity retention of 92% at 1C (Figure S3) and 86% at 5C after 200 and 1000 cycles, respectively (Figure 2c). It also displayed excellent structural integrity and morphology retention upon continuous cycling as deduced from its XRD and SEM results (Figures S4 and S5). The rate-performances of NaNbAl anode were assessed at various C-rates. It delivered charge capacities of 125, 120, 113, 106, 98, 85, and 65 mAh g^{-1} at C/10, C/5, C/2, 1C, 2C, 5C, and 10C, respectively (Figure 2d and Figure S6). To investigate the Na^+ (de)insertion kinetics into the NaNbAl anode material, we performed the galvanostatic intermittent titration technique (GITT) (Figure S7a,b). From the GITT experiment, we have obtained the Na^+ diffusion coefficient (D_{Na^+}) values in the range of 10^{-10}–10^{-11} cm^2 s^{-1}, which suggests good Na ion diffusivity even in the bulk state (Figure 2e) [30–32]. Al^{3+} substitution not only lightens the molecular weight but also stabilizes the NASICON framework, enabling highly reversible $Nb^{5+}/Nb^{4+}/Nb^{3+}$ redox activity [19].

To gain a deeper understanding of Na-ion (de)intercalation into the NaNbAl anode, we conducted *operando* X-ray diffraction (XRD) measurements at a C/10 rate in a lab-scale X-ray diffractometer (Figure 3a, Figure S8). At C/10 rate, as the anode discharged to 0.9 V, we observed a gradual shift of peaks, including (104), (110), (113), toward lower 2θ values, indicating the formation of a complete solid solution. The c-parameter varies minimally ($\Delta c/c$ = +0.008 %), whereas the a-parameter shows significant changes ($\Delta a/a$ = +1.51%) (Figure S9). It implies that the Na-ions get predominantly filled into Na(2) sites, leading to the increase of a-parameter. Importantly, the anode undergoes

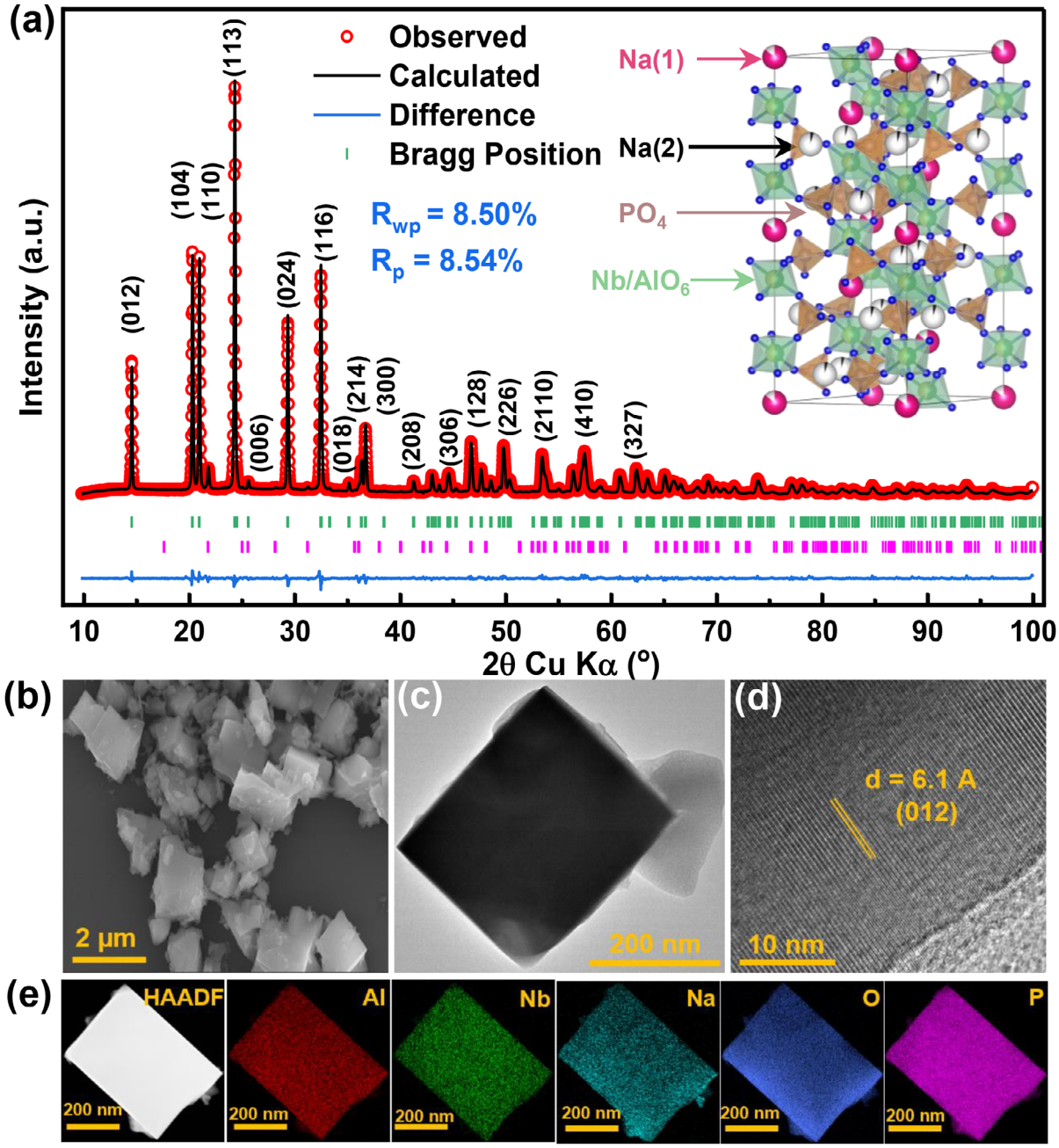

FIGURE 1 | (a) Rietveld-refined XRD pattern (Green Bragg Ticks: $NaNbAl(PO_4)_3$; Pink Bragg Ticks: $AlPO_4$); inset shows the crystal structure of NaNbAl anode. (b) SEM, (c) low-magnification TEM, (d) high-resolution TEM (HRTEM), and (e) HAADF-STEM images with corresponding elemental mapping of the NaNbAl anode.

smoother volume expansion of 6.2% during the Na-ion insertion. Upon subsequent charging, these reflections reverted to their original positions, confirming structural robustness and higher reversibility of $Nb^{5+}/Nb^{4+}/Nb^{3+}$ redox processes. Note that the irreversible loss of Na-ions (~1.1 moles pfu) during the first cycle is attributable to the formation of SEI.

Ex situ magic angle spinning (MAS) NMR measurements were conducted on NaNbAl anode at different states of charge during the first cycle. The filling of Na(1) and Na(2) sites was estimated using deconvolution in Figure 3b and Figure S10b. At least four different NMR signals are noticed in the range of −40 to 0 ppm that are attributable to different Na(1) environments (Figure S11a) [19]. The NMR peak spanning from 0 to 15 ppm is ascribed to Na(2) site. The total Na content in the pristine anode is estimated as ~0.96 moles *pfu*, in agreement with our XRD results. As the NaNbAl anode is discharged to 0.9 V, we observe predominant filling of Na(2) site, leading to ~2.7 moles of Na-ion *pfu* in total. On the subsequent charge, the NMR spectrum almost recovers to its original state, confirming the complete reversibility of the Na (de)intercalation reaction.

To monitor the changes in the oxidation state of the Nb redox center throughout the cycling process, we conducted X-ray absorption spectroscopy (XAS) measurements at various states of charge of NaNbAl. The corresponding normalized ex situ XANES

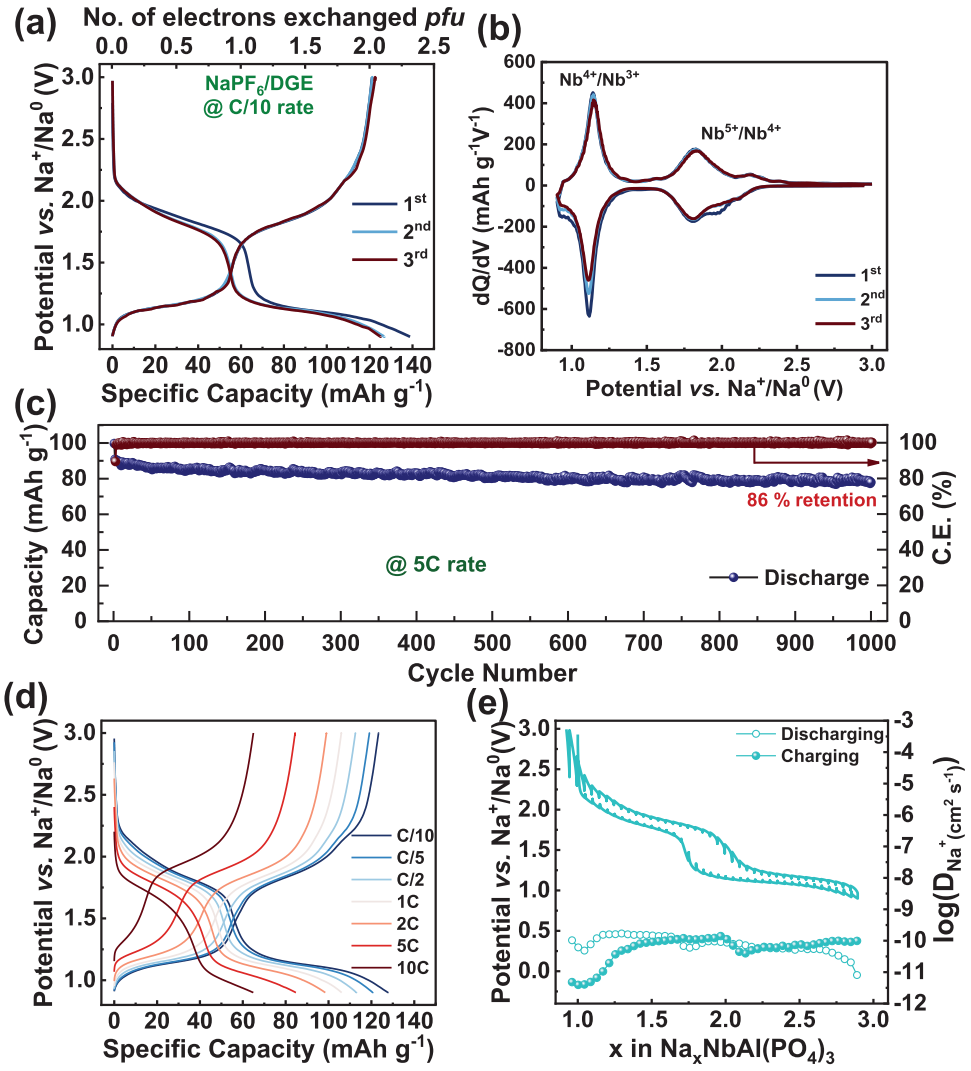

FIGURE 2 | (a) Galvanostatic voltage-capacity and (b) corresponding differential capacity (dQ/dV) profiles of the NaNbAl anode recorded at a C/10 rate (1C = 122 mAh g^{-1}). (c) Long-term cycling stability was evaluated at a high current rate of 5C. (d) Voltage-capacity profiles obtained at various C-rates ranging from C/10 to 10C, highlighting the rate capability of the anode. (e) Galvanostatic intermittent titration technique (GITT) voltage profile with the calculated Na^+ diffusion coefficient ($D_{Na}{}^+$) plotted as a function of the number of electrons exchanged during (de)sodiation of the NaNbAl anode.

spectra collected at the Nb edge are shown in Figure 3c and Figure S11a. When discharged to 1.5 V, the Nb K-edge shifts from higher to lower energy (19 003.6 to 19 000.2 eV), indicating the reduction of Nb^{5+} to Nb^{4+} due to Na-ion intercalation. Subsequent discharge of the NaNbAl anode to 0.9 V results in the Nb K-edge moving to an even lower energy of 18998.5 eV, signifying the additional reduction of Nb^{4+} to Nb^{3+} (Figure S11b). During the subsequent charge, the Nb K-edge returns to its original position, demonstrating the complete reversibility of the $Nb^{5+}/Nb^{4+}/Nb^{3+}$ redox process during Na (de)intercalation process [18, 28]. Additionally, ex situ XPS measurement (Figure S12) on the pristine anode reveals the presence of Nb^{5+}, indicated by the observation of doublet peaks for Nb $3d_{3/2}$ and Nb $3d_{5/2}$ at binding energies of 211.2 and 208.5 eV, respectively [33]. As the anode discharges to 1.5 V, these peaks shift to lower binding energies of 210.6 and 207.9 eV, suggesting a conversion to Nb^{4+}. Further discharging to 0.9 V results in additional shifts to 209.5 and 206.7 eV for the Nb $3d_{3/2}$ and Nb $3d_{5/2}$ peaks, respectively, indicating the presence of Nb^{3+}. Upon charging to 3.0 V, the core-level Nb 3d peaks return to their original positions, illustrating the excellent reversibility of the NaNbAl anode during Na-ion storage.

The Fourier transform (FT) of the extended X-ray absorption fine structure (EXAFS) oscillations, along with their theoretical fits collected at the Nb-edge, are illustrated in Figure 3d. The prominent peak at ~1.53 Å signifies the first coordination shell, corresponding to the $(Nb/Al)O_6$ shell. Notably, the EXAFS data acquired at the conclusion of the discharge process exhibit a shift toward higher R values, indicative of the expansion of the NaNbAl anode owing to the intercalation of sodium ions into the lattice structure. Conversely, upon subsequent charging, the spectra revert to lower R values that closely resemble those of the pristine state, suggesting the reversible (de)intercalation of sodium ions. This phenomenon is attributed to the redox reversibility of $Nb^{5+}/Nb^{4+}/Nb^{3+}$, aligning well with our electrochemical and

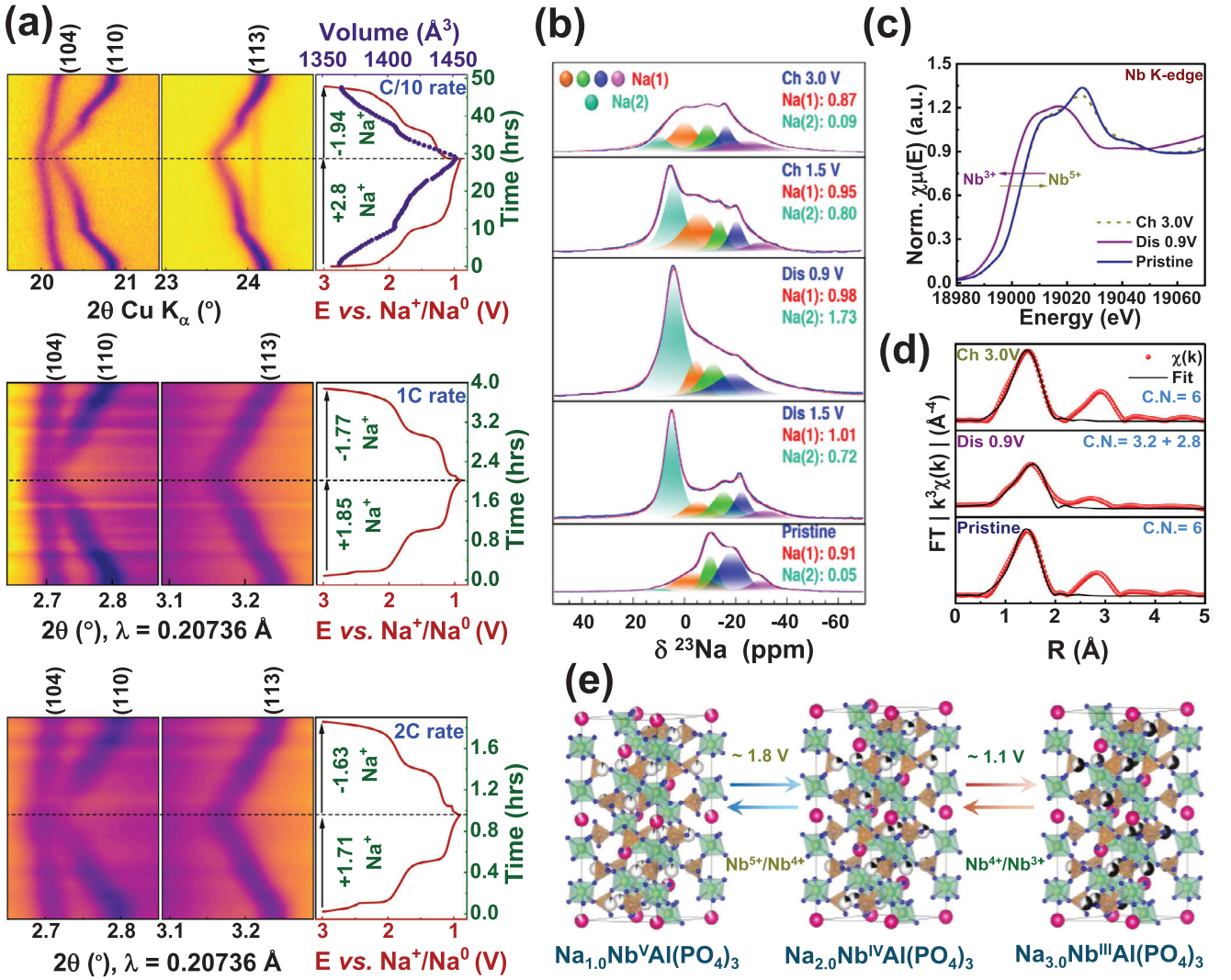

FIGURE 3 | (a) Intensity contour maps of *operando* XRD patterns for the NaNbAl anode collected at different C-rates. (b) Ex situ ^{23}Na MAS NMR spectra with quantitative deconvolution of Na(1) and Na(2) sites. (c) Ex situ XANES and (d) FT-EXAFS plots of the NASICON-NaNbAl anode collected at the Nb K-edge. (e) Schematic illustration of the Na-ion (de)intercalation mechanism in the NaNbAl anode.

in situ XRD analyses. The EXAFS fitting parameters for the pristine, discharged, and charged electrodes are detailed in Table S2. The EXAFS analysis of the first coordination shell for the pristine NaNbAl anode reveals an ideal Nb/AlO_6 octahedral configuration, with all six Nb-O bonds exhibiting the same length of ~1.97 Å. In contrast, the EXAFS data for the discharged NaNbAl electrode can be adequately fitted using a [3.2+2.8] coordination model, resulting in an octahedral distortion characterized by $\Delta \approx 9.96 \times 10^{-4}$ (Figure S13a). This finding suggests a minimal Jahn-Teller distortion, which arises from the expansion of the NASICON framework due to sodium-ion intercalation [34–37]. Various coordination models, including [6+0], [5+1], [4+2], and [3+3] were examined, yet the [3.2+2.8] model provided the optimal fit (Figure S13b). Unlike the presence of shortened vanadyl (V=O) bonds resulting from dπ-pπ bonding within VO_6 octahedra, which causes distortion of the VO_6 structure [22, 23], no such short Nb = O bonds are observed in the NbO_6 octahedra. This absence is attributed to the ineffective or nearly impossible dπ-pπ bonding between the 4d orbitals of Nb and the 2p orbitals of O [38, 39]. Furthermore, the EXAFS data for the charged NaNbAl anode indicate a return to the undistorted (Nb/Al)O_6 configuration, thereby confirming the excellent structural stability of the NASICON framework. This suggests that the greater electropositivity of Nb cations and the substitution of the electrochemically inactive and lighter Al^{3+} ions foster the formation of robust covalent bonds with oxygen, thereby minimizing Nb/AlO_6 distortion and enhancing framework stability during Na-ion (de)intercalation [26].

Further, we followed the sodium ion (de)intercalation mechanism of NaAlNb anode at faster current rates using synchrotron XRD. The contour plots of *operando* XRD measurements of the NaNbAl anode at 1C and 2C rates (collected during the second cycle) are displayed in Figure 3a and Figure S14. During the discharge/charge, the NaNbAl anode (de)intercalates 1.85/1.77 and 1.71/1.63 sodium ions *pfu* at 1C and 2C, respectively, though solid-solution formation (which is akin to C/10 rate). These observations underscore the higher rate kinetics of the bulk NaNbAl demonstrating its ability to rapidly and reversibly (de)intercalate sodium ions under higher current rates. Overall, the NaNbAl

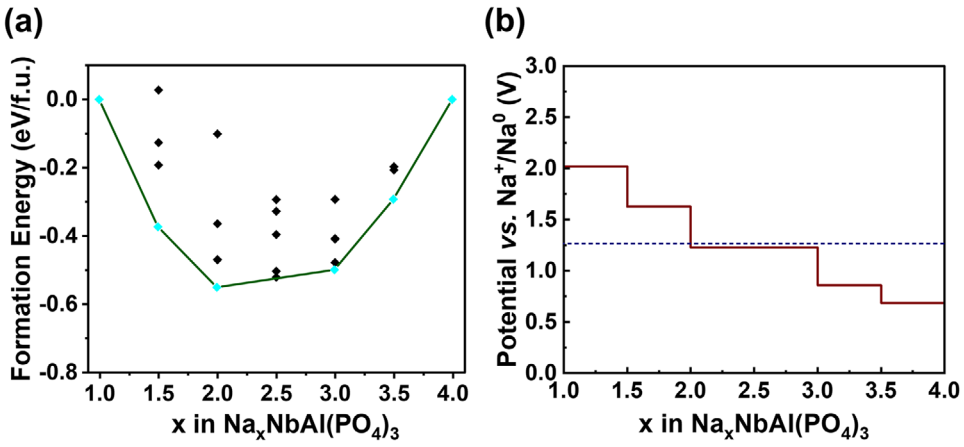

FIGURE 4 | (a) DFT-calculated formation energies of NaNbAl anode as a function of the Na content (x). Black symbols represent the formation energies of all enumerated Na/vacancy configurations, while the cyan points connected by wine lines denote the ground-state configurations forming the 0 K convex hull. (b) Corresponding Na (de)intercalation voltage profile derived from the convex hull, plotted versus x. The step-like voltage plateaus reflect two-phase reactions between adjacent ground-state compositions, and the dashed horizontal line indicates the average Na intercalation voltage over the entire Na composition range (i.e., $1 \leq x \leq 4$).

anode (de)intercalates nearly two moles of sodium ions *pfu via* the reversible operation of Nb^{5+}/Nb^{4+} (~1.8 V) and Nb^{4+}/Nb^{3+} (~1.1 V) across different current rates (Figure 3d).

To understand the phase behavior and electronic structure of the NaNbAl anode as a function of Na content, we performed several DFT calculations, with methodological details compiled in the Supporting Information. Specifically, we calculated the pseudo-binary convex hull with Na composition change (x) in NaNbAl at 0 K, and the corresponding Na (de)intercalation voltage profile and plotted them in panels a and b of Figure 4. Importantly, we observe ground state configurations at Na compositions of x = 1.5, 2, 3, and 3.5 apart from the end-member compositions of x = 1 and x = 4 (Figure 4a). Thus, at 0 K, the NaNbAl system should exhibit two-phase equilibria across x = 1–1.5, 1.5–2, 2–3, 3–3.5, and 3.5–4, with the corresponding voltage plateaus illustrated in Figure 4b. However, the ground states occurring at x = 1.5 and 3.5 are 'shallower' compared to the ground states at x = 2 and 3, as also indicated by the 'small' voltage drops at x = 1.5 and 3.5 in Figure 4b. This suggests that under room temperature operating conditions, there may be a solid-solution-like behavior across the $1 \leq x \leq 2$ and $3 \leq x \leq 4$ composition ranges, instead of observing the ground state configurations at x = 1.5 and 3.5, in general agreement with the observed electrochemical voltage profiles measured in Figure 2a. Additionally, the calculated average Na (de)intercalation voltage, ~1.3 V versus Na (Figure 4b), is also in good agreement with the observed average voltage during cycling in Figure 2a.

We also examined the DFT-calculated electronic density of states (DOS) to obtain insights into the changes in the Nb oxidation state (and redox behavior) with Na (de)intercalation in the NaNbAl anode, with the DOS plots compiled in Figure S15 of the Supporting Information. Importantly, we found that the Nb *d* states are completely pushed into the conduction band at the pristine composition of $NaNbAl(PO_4)_3$, indicating the presence of the Nb^{5+} oxidation state in the structure. Subsequently, as Na is added into the structure, the Nb *d* states consistently shift to the valence band (i.e., below the Fermi level), indicating a gradual reduction of the Nb^{5+} to Nb^{4+}, Nb^{3+}, and finally Nb^{2+}. A full reduction of all Nb atoms in the NaNbAl structure also coincides with the presence of the calculated 'deep' ground state configurations (Figure 4a) at x = 2 (Nb^{4+}), x = 3 (Nb^{3+}), and x = 4 (Nb^{2+}). Thus, incorporation of Al in NaNbAl enables the clear demarcation of Nb redox behavior with Na content, thereby potentially improving reversible redox behavior.

Interestingly, we observe a significant drop in the calculated band gap (E_g) of the NaNbAl material, from ~2.48 to 0.08 eV, as the Na content changes from x = 1 to 1.5. This drop in E_g also coincides with the gap separating the Nb *d* states at x = 1.5 (Figure S15b) instead of separating the O *p* states and Nb *d* states at x = 1 (Figure S15a). Moreover, the calculated gap continues to remain low (E_g ~0.21–0.23 eV) as Nb reduces with increasing Na content, with a final increase in E_g to 0.87 eV at x = 4, corresponding to a complete reduction of Nb^{3+} to Nb^{2+}. Thus, we observe that incorporating Al reduces the E_g in NASICON-NaNbAl, potentially enhancing electronic transport compared to NASICON with only Nb, which could lead to improved cycling behavior.

To further quantify the Na^+ diffusion kinetics in the NaNbAl anode, we performed DFT-based NEB calculations at x = 1, 2, and 3 compositions, and plotted the migration energy pathways (MEPs) in panels a, b, and c, respectively, of Figure 5. We considered the Na(1)→Na(2) migration pathway in all our DFT-NEB calculations, where Na(1) and Na(2) are the distinct Na sites available in the NASICON structure. Importantly, our calculated migration barriers (E_m) are 427, 171, and 150 meV at x = 1, 2, and 3, respectively, highlighting facile Na motion in the NaNbAl structure across Na compositions, which should result in better electrochemical reversibility. Note that the Na migration process in NaSICON structures is generally an 'uphill' (or 'downhill') trajectory, with the E_m largely reflecting the site energy differences between the Na(1) and Na(2) sites [40–42]. Thus, lower site energy differences between the Na(1) and Na(2) sites should result in lower E_m. Indeed, the 'low' E_m values at x = 2 (Figure 4d) and x = 3 (Figure 4e) can be largely attributed to the 'low' site energy differences between the Na(1) and Na(2) sites, as highlighted

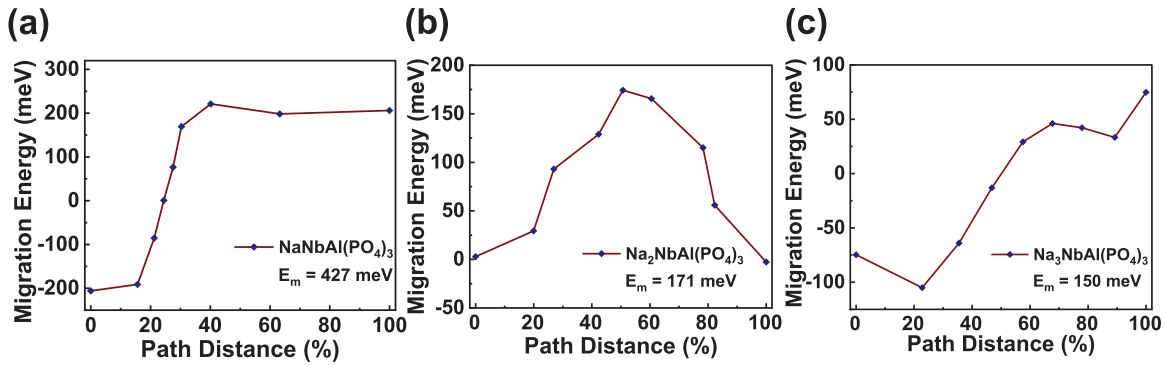

FIGURE 5 | DFT-NEB calculated Na^+ MEPs along the Na(1)→Na(2) diffusion pathway in $Na_xNbAl(PO_4)_3$ for (a) x = 1, (b) x = 2, and (c) x = 3 compositions. The MEP is plotted as a function of the normalized path distance, where 0% and 100% correspond to the initial Na(1) site and the final Na(2) site, respectively. The migration barriers (E_m) are 427, 171, and 150 meV for x = 1, 2, and 3, respectively.

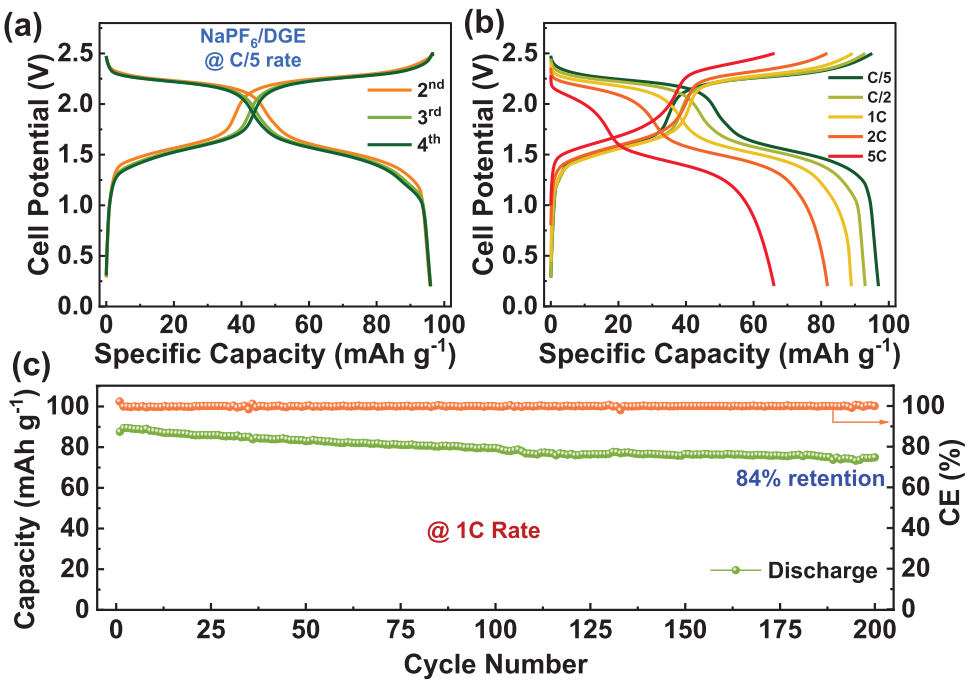

FIGURE 6 | (a) Charge-discharge profiles, (b) rate capability, and (c) long-term cycling performance of the Na_4VP||NaNbAl full sodium-ion cell.

by the corresponding energy values at the 0% and 100% path distances, respectively, which can be a result of Al incorporation within the NASICON structure. Thus, Al addition to the Nb-based NASICON structure can cause an improvement in the Na diffusion kinetics, thereby enabling reversible electrochemical Na (de)intercalation at high rates.

Finally, we proceeded with the fabrication of a full Na-ion cell by pairing NASICON-$Na_4V_2(PO_4)_3$ (Na_4VP) as the cathode and NaNbAl as the anode. To compensate for the loss of Na-ions during the formation of SEI on the NaNbAl anode, we electrochemically pre-sodiated the $Na_3V_2(PO_4)_3$ cathode to obtain $Na_4V_2(PO_4)_3$ (Na_4VP) (for details, see the Experimental details), which was then paired with the anode to fabricate the full Na-ion cell [19, 43–45]. Figure 6a shows the charge-discharge profiles of the Na_4VP||NaNbAl full cell. The Na_4VP||NaNbAl full cell delivers first cycle charge and discharge capacities of 154 and 88 mAh g^{-1}, respectively, resulting in an initial coulombic efficiency (ICE) of 57% (Figure S16). From the second cycle onward, the full cell exhibits reversible capacities of 96 mAh g^{-1} (based on the weight of the cathode) with an average cell voltage of 2.1 V, yielding an energy density of approximately 201 Wh kg^{-1} (based on the weight of the cathode). The full Na-ion cell delivers charge capacities of 96.2, 93.1, 89.3, 81.8, and 66.2 mAh g^{-1} at rates of C/5, C/2, 1C, 2C, and 5C, respectively. When the current density is reversed back to C/5, the full cell nearly recovers its original discharge capacity (Figure 6b, Figure S17). Further, at 1C rate, the Na_4VP||NaNbAl cell retains 84% of its initial capacity after 200 cycles (Figure 6c).

3 | Conclusion

In conclusion, we demonstrated highly reversible $Nb^{5+}/Nb^{4+}/Nb^{3+}$ redox reactions and good electrochemical performance in the bulk NASICON-$NaNbAl(PO_4)_3$ anode, even at higher C-rates,

in comparison to other Nb and V-based NASICON anodes (Table S3). Our combined electrochemical and operando XRD measurements exhibited faster Na-ion (de)intercalation kinetics into bulk $NaNbAl(PO_4)_3$ anode through solid-solution formation, as confirmed with DFT-based calculations. We can tentatively attribute the rapid Na-ion intercalation kinetics to the formation of different Na(1) environments (as observed by NMR), which have closer site energies [46] and can thereby enhance ion mobility, in agreement with the DFT-calculated E_m. A full Na-ion cell (Na_4VP||NaNbAl) was also built, which retained 84% capacity after 200 cycles. It is worth noting that a similar anode was recently reported for good electrochemical performance, but with carbon-coating and nano-scale particles [28]. Yet, achieving faster Na-ion insertion kinetics in bulk NASICON electrodes opens new possibilities of building high-energy density and high-rate capability SIBs [47].

Acknowledgements

This work was supported by the Science and Engineering Research Board, Department of Science & Technology (DST), Government of India (IPA/2021/000007). S.K.J. acknowledges the Institute of Eminence (IoE) grant, Indian Institute of Science (IE/CARE-21-0330, IE/RERE-21-0569), and the Core Research Grant by Science and Engineering Research Board (SERB), India (CRG/2022/007365). A.P. and B.P. thank JNCASR and CSIR for the research fellowship. The authors acknowledge DESY (Hamburg, Germany), a member of the Helmholtz Association HGF, for the provision of experimental facilities. Parts of this research were carried out at PETRA III, and the authors thank Dr. Volodymyr Baran for his assistance in using Beamline P02.1 to perform in situ XRD measurements and Dr. Edmund Welter for his assistance in using Beamline P65 to perform X-ray absorption spectroscopy measurements. Beamtime was allocated for proposal I-20240406 and I-20250447. Financial support by the DST provided within the framework of the India@DESY collaboration is gratefully acknowledged.

Conflicts of Interest

The authors declare no conflicts of interest.

Data Availability Statement

The data that support the findings of this study are available from the corresponding author upon reasonable request.

References

1. Z. Yang, J. Zhang, M. C. W. Kintner-Meyer, et al., "Electrochemical Energy Storage for Green Grid," *Chemical Reviews* 111 (2011): 3577–3613, https://doi.org/10.1021/cr100290v.

2. P. K. Nayak, L. Yang, W. Brehm, and P. Adelhelm, "From Lithium-Ion to Sodium-Ion Batteries: Advantages, Challenges, and Surprises," *Angewandte Chemie International Edition* 57 (2018): 102–120, https://doi.org/10.1002/anie.201703772.

3. K. Kubota, S. Kumakura, Y. Yoda, K. Kuroki, and S. Komaba, "Electrochemistry and Solid-State Chemistry of $NaMeO_2$ (Me = 3d Transition Metals)," *Advanced Energy Materials* 8 (2018): 1703415, https://doi.org/10.1002/aenm.201703415.

4. Y. Lu, L. Wang, J. Cheng, and J. B. Goodenough, "Prussian blue: A new framework of electrode materials for sodium batteries," *Chemical Communications* 48 (2012): 6544–6546, https://doi.org/10.1039/c2cc31777j.

5. P. Barpanda, L. Lander, S. I. Nishimura, and A. Yamada, "Polyanionic Insertion Materials for Sodium-Ion Batteries," *Advanced Energy Materials* 8 (2018): 1703055, https://doi.org/10.1002/aenm.201703055.

6. W. Zhang, L. He, J. Li, et al., "Configurational Entropy-Tailored NASICON Cathode Redox Chemistry for Capacity-Dense And Ultralong Cyclability," *Energy & Environmental Science* 18 (2025): 7278–7290, https://doi.org/10.1039/D5EE00877H.

7. W. Zhang, Y. Wu, Y. Dai, et al., ""Mn-locking" Effect By Anionic Coordination Manipulation Stabilizing Mn-Rich Phosphate Cathodes," *Chemical Science* 14 (2023): 8662–8671, https://doi.org/10.1039/D3SC03095D.

8. E. Irisarri, A. Ponrouch, and M. R. Palacin, "Review—Hard Carbon Negative Electrode Materials for Sodium-Ion Batteries," *Journal of The Electrochemical Society* 162 (2015): A2476–A2482, https://doi.org/10.1149/2.0091514jes.

9. B. Xiao, T. Rojo, and X. Li, "Hard Carbon as Sodium-Ion Battery Anodes: Progress and Challenges," *Chemsuschem* 12 (2019): 133–144, https://doi.org/10.1002/cssc.201801879.

10. Z. Li, Z. Jian, X. Wang, I. A. Rodríguez-Pérez, C. Bommier, and X. Ji, "Hard Carbon Anodes Of Sodium-Ion Batteries: Undervalued Rate Capability," *Chemical Communications* 53 (2017): 2610–2613, https://doi.org/10.1039/C7CC00301C.

11. P. Senguttuvan, G. Rousse, M. E. Arroyo Y De Dompablo, H. Vezin, J. M. Tarascon, and M. R. Palacín, "Low-Potential Sodium Insertion in a NASICON-Type Structure Through the Ti(III)/Ti(II) Redox Couple," *Journal of the American Chemical Society* 135 (2013): 3897–3903, https://doi.org/10.1021/ja311044t.

12. T. Akçay, M. Häringer, K. Pfeifer, et al., "$Na_3V_2(PO_4)_3$—A Highly Promising Anode and Cathode Material for Sodium-Ion Batteries," *ACS Applied Energy Materials* 4 (2021): 12688–12695.

13. Z. Jian, Y. Sun, and X. Ji, "A New Low-Voltage Plateau of $Na_3V_2(PO_4)_3$ as an Anode for Na-Ion Batteries," *Chemical Communications* 51 (2015): 6381–6383, https://doi.org/10.1039/C5CC00944H.

14. B. Patra, R. Hegde, A. Natarajan, et al., "Stabilizing Multi-Electron NASICON-$Na_{1.5}V_{0.5}Nb_{1.5}(PO_4)_3$ Anode via Structural Modulation for Long-Life Sodium-Ion Batteries," *Advanced Energy Materials* 14 (2024): 2304091, https://doi.org/10.1002/aenm.202304091.

15. N. R. Khasanova, R. V. Panin, I. R. Cherkashchenko, M. V. Zakharkin, D. A. Novichkov, and E. V. Antipov, "$NaNbV(PO_4)_3$: Multielectron NASICON-Type Anode Material for Na-Ion Batteries With Excellent Rate Capability," *ACS Applied Materials & Interfaces* 15 (2023): 30272–30280, https://doi.org/10.1021/acsami.3c04576.

16. R. V. Panin, I. R. Cherkashchenko, V. V. Zaitseva, et al., "Realizing Three-Electron Redox Reactions in NASICON-Type $NaCrNb(PO_4)_3$ for Sodium Ion Battery Applications," *Chemistry of Materials* 36 (2024): 6902–6911, https://doi.org/10.1021/acs.chemmater.4c00933.

17. Y. Fang, L. Xiao, J. Qian, et al., "3D Graphene Decorated $NaTi_2(PO_4)_3$ Microspheres as a Superior High-Rate and Ultracycle-Stable Anode Material for Sodium Ion Batteries," *Advanced Energy Materials* 6 (2016): 1502197, https://doi.org/10.1002/aenm.201502197.

18. B. Patra, K. Kumar, D. Deb, S. Ghosh, G. S. Gautam, and P. Senguttuvan, "Unveiling a High Capacity Multi-Redox ($Nb^{5+}/Nb^{4+}/Nb3^{+}$) NASICON-$Nb_2(PO_4)_3$ Anode for Li- and Na-ion Batteries," *Journal of Materials Chemistry A* 11 (2023): 8173–8183, https://doi.org/10.1039/D2TA05971A.

19. B. Patra, S. Narayanan, S. Halder, et al., "NASICON-$NaV_{0.25}Al_{0.25}Nb_{1.5}(PO_4)_3$/C: A High-Rate and Robust Anode for Fast Charging and Long-Life Sodium-Ion Batteries," *Advanced Materials* 37 (2025): 2419417, https://doi.org/10.1002/adma.202419417.

20. R. Liu, G. Xu, Q. Li, et al., "Exploring Highly Reversible 1.5-Electron Reactions ($V^{3+}/V^{4+}/V^{5+}$) in $Na_3VCr(PO_4)_3$ Cathode for Sodium-Ion Batteries," *ACS Applied Materials & Interfaces* 9 (2017): 43632–43639, https://doi.org/10.1021/acsami.7b13018.

21. F. Lalère, V. Seznec, M. Courty, R. David, J. N. Chotard, and C. Masquelier, "Improving the Energy Density of $Na_3V_2(PO_4)_3$-Based Positive Electrodes Through V/Al Substitution," *Journal of Materials Chemistry A* 3 (2015): 16198–16205.

22. S. Park, J. N. Chotard, D. Carlier, et al., "Irreversible Electrochemical Reaction at High Voltage Induced by Distortion of Mn and V Structural Environments in Na_4 $MnV(PO_4)_3$," *Chemistry of Materials* 35 (2023): 3181–3195, https://doi.org/10.1021/acs.chemmater.2c03787.

23. S. Park, J. N. Chotard, D. Carlier, et al., "Crystal Structures and Local Environments of NASICON-Type $Na_3FeV(PO_4)_3$ and $Na_4FeV(PO_4)_3$ Positive Electrode Materials for Na-Ion Batteries," *Chemistry of Materials* 33 (2021): 5355–5367, https://doi.org/10.1021/acs.chemmater.1c01457.

24. R. Liu, S. Zheng, Y. Yuan, et al., "Counter-Intuitive Structural Instability Aroused By Transition Metal Migration in Polyanionic Sodium Ion Host," *Advanced Energy Materials* 11 (2021): 2003256.

25. Y. Liu, X. Rong, R. Bai, et al., "Identifying the Intrinsic Anti-Site Defect in Manganese-Rich NASICON-Type Cathodes," *Nature Energy* 8 (2023): 1088–1096, https://doi.org/10.1038/s41560-023-01301-z.

26. Y. Xin, Y. Wang, Q. Zhou, et al., "The Importance of Bond Covalency for the Activation of Multielectron Reactions In Phosphate Cathodes for Sodium-Ion Batteries," *Energy Storage Materials* 72 (2024): 103770, https://doi.org/10.1016/j.ensm.2024.103770.

27. K. K. Rangan, "$AMVMIII(PO_4)_3$: New Mixed-Metal Phosphates Having NASICON and Related Structures," *Inorganic Chemistry* 34 (1995): 1969–1972, https://doi.org/10.1021/ic00111a055.

28. I. R. Cherkashchenko, R. V. Panin, A. V. Babkin, D. A. Novichkov, E. V. Antipov, and N. R. Khasanova, "$NaAlNb(PO_4)_3$ NASICON-type Phosphate With the $Nb^{5+}Nb^{4+}Nb^{3+}$ Multielectron Redox Activity on Sodium Intercalation," *Mendeleev Communications* 35 (2025): 393–395, https://doi.org/10.71267/mencom.7637.

29. L. Znaidi, S. Launay, and M. Quarton, "Crystal Chemistry and Electrical Properties of $Na_{1+x}ScNb(PO_4)_3$ Phases," *Solid State Ionics* 93 (1997): 273–277, https://doi.org/10.1016/S0167-2738(96)00558-9.

30. X. Jiang, T. Zhang, and J. Y. Lee, "Does Size Matter—What Other Factors are Limiting the Rate Performance of $Na_3V_2(PO_4)_3$ Cathode In Sodium-Ion Batteries," *Journal of Power Sources* 372 (2017): 91–98, https://doi.org/10.1016/j.jpowsour.2017.10.075.

31. Q. Ni, Y. Bai, Y. Li, et al., "3D Electronic Channels Wrapped Large-Sized $Na_3V_2(PO_4)_3$ as Flexible Electrode for Sodium-Ion Batteries," *Small* 14 (2018): 1702864, https://doi.org/10.1002/smll.201702864.

32. M. Li, L. Liu, P. Wang, J. Li, Q. Leng, and G. Cao, "Highly Reversible Sodium-ion Storage in $NaTi_2(PO_4)_3$/C Composite Nanofibers," *Electrochimica Acta* 252 (2017): 523–531, https://doi.org/10.1016/j.electacta.2017.09.020.

33. Z. Wu, L. Jiang, W. Tian, et al., "Novel Sub-5 nm Layered Niobium Phosphate Nanosheets for High-Voltage, Cation-Intercalation Typed Electrochemical Energy Storage in Wearable Pseudocapacitors," *Advanced Energy Materials* 9 (2019): 1900111, https://doi.org/10.1002/aenm.201900111.

34. G. L. Miessler, P. J. Fischer, and D. A. Tarr, *Inorganic Chemistry*, 5th ed. (Pearson Education, 2013).

35. M. A. Halcrow, "Jahn–Teller Distortions in Transition Metal Compounds, and Their Importance in Functional Molecular and Inorganic Materials," *Chemical Society Reviews* 42 (2013): 1784–1795, https://doi.org/10.1039/C2CS35253B.

36. R. D. Shannon, P. S. Gumerman, and J. Chenavas, "Effect of Octahedral Distortion on Mean Mn^{3+}-O Distances," *American Mineralogist* 60 (1975): 714–716.

37. M. W. Lufaso and P. M. Woodward, "Jahn–Teller Distortions, Cation Ordering and Octahedral Tilting in Perovskites," *Acta Crystallographica Section B Structural Science* B60 (2004): 10–20, https://doi.org/10.1107/S0108768103026661.

38. J. M. Mayer, "Metal-Oxygen Multiple Bond Lengths: A Statistical Study," *Inorganic Chemistry* 27 (1988): 3899–3903, https://doi.org/10.1021/ic00295a006.

39. F. A. Cotton and G. Wilkinson, *Advanced Inorganic Chemistry*, 5th ed. (Wiley, 1988).

40. Z. Wang, T. P. Mishra, W. Xie, et al., "Kinetic Monte Carlo Simulations of Sodium Ion Transport in NaSICON Electrodes," *ACS Materials Letters* 5 (2023): 2499–2507, https://doi.org/10.1021/acsmaterialslett.3c00610.

41. D. B. Tekliye, A. Kumar, W. Xie, T. D. Mercy, P. Canepa, and G. S. Gautam, "Exploration of NaSICON Frameworks as Calcium-Ion Battery Electrodes," *Chemistry of Materials* 34 (2022): 10133–10143, https://doi.org/10.1021/acs.chemmater.2c02841.

42. Z. Deng, T. P. Mishra, E. Mahayoni, et al., "Fundamental Investigations on the Sodium-Ion Transport Properties of Mixed Polyanion Solid-State Battery Electrolytes," *Nature Communications* 13 (2022): 4470, https://doi.org/10.1038/s41467-022-32190-7.

43. M. Xu, F. Zhang, Y. Zhang, et al., "Controllable synthesis of a Na-enriched $Na_4V_2(PO_4)_3$ Cathode for High-Energy Sodium-Ion Batteries: A Redox-Potential-Matched Chemical Sodiation Approach," *Chemical Science* 14 (2023): 12570–12581, https://doi.org/10.1039/D3SC03498D.

44. S. Mirza, Z. Song, H. Zhang, A. Hussain, H. Zhang, and X. Li, "A Simple Pre-Sodiation Strategy to Improve the Performance and Energy Density of Sodium Ion Batteries With $Na_4V_2(PO_4)_3$ as the Cathode Material," *Journal of Materials Chemistry A* 8 (2020): 23368–23375, https://doi.org/10.1039/D0TA08186H.

45. Y. Liu, X. Wu, A. Moeez, et al., "Na-Rich $Na_3V_2(PO_4)_3$ Cathodes for Long Cycling Rechargeable Sodium Full Cells," *Advanced Energy Materials* 13 (2023): 2203283, https://doi.org/10.1002/aenm.202203283.

46. Y. Zeng, B. Ouyang, J. Liu, et al., "High-Entropy Mechanism to Boost Ionic Conductivity," *Science* 378 (2022): 1320–1324, https://doi.org/10.1126/science.abq1346.

47. R. Jain, A. S. Lakhnot, K. Bhimani, et al., "Nanostructuring Versus Microstructuring in Battery Electrodes," *Nature Reviews Materials* 7 (2022): 736–746, https://doi.org/10.1038/s41578-022-00454-9.

Supporting Information

Additional supporting information can be found online in the Supporting Information section.

Supporting File: smll72691-sup-0001-SuppMat.docx.